

ChA-MAEViT: Unifying Channel-Aware Masked Autoencoders and Multi-Channel Vision Transformers for Improved Cross-Channel Learning

Chau Pham
Boston University
chaupham@bu.edu

Juan C. Caicedo
University of Wisconsin-Madison
juan.caicedo@wisc.edu

Bryan A. Plummer
Boston University
bplum@bu.edu

Abstract

Prior work using Masked Autoencoders (MAEs) typically relies on random patch masking based on the assumption that images have significant redundancies across different channels, allowing for the reconstruction of masked content using cross-channel correlations. However, this assumption does not hold in Multi-Channel Imaging (MCI), where channels may provide complementary information with minimal feature overlap. Thus, these MAEs primarily learn local structures within individual channels from patch reconstruction, failing to fully leverage cross-channel interactions and limiting their MCI effectiveness. In this paper, we present ChA-MAEViT, an MAE-based method that enhances feature learning across MCI channels via four key strategies: (1) dynamic channel-patch masking, which compels the model to reconstruct missing channels in addition to masked patches, thereby enhancing cross-channel dependencies and improving robustness to varying channel configurations; (2) memory tokens, which serve as long-term memory aids to promote information sharing across channels, addressing the challenges of reconstructing structurally diverse channels; (3) hybrid token fusion module, which merges fine-grained patch tokens with a global class token to capture richer representations; and (4) Channel-Aware Decoder, a lightweight decoder utilizes channel tokens to effectively reconstruct image patches. Experiments on satellite and microscopy datasets, CHAMMI, JUMP-CP, and So2Sat, show that ChA-MAEViT significantly outperforms state-of-the-art MCI-ViTs by 3.0-21.5%, highlighting the importance of cross-channel interactions in MCI.

1. Introduction

Visual encoders generally process fixed-channel inputs, such as RGB, during both training and testing phases [25, 29, 32–34, 42, 46, 47]. However, in many applications like satellite imaging [56], robotic sensing [57], cell microscopy [6, 13], and medical imaging [9], the input data

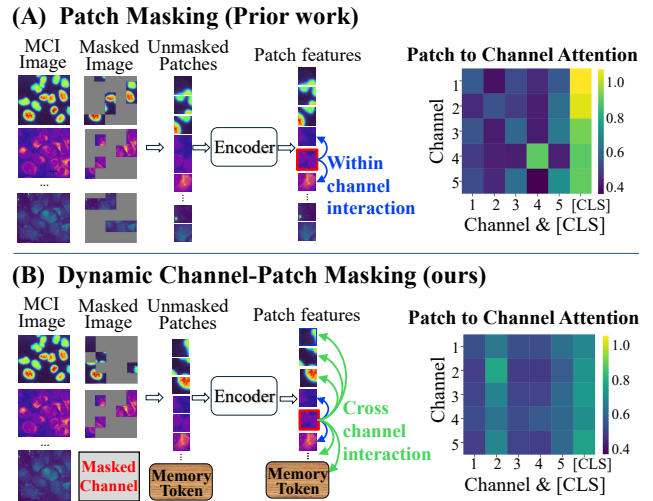


Figure 1. **Image patch interactions in MCI.** (A) **Prior Work on MCI-MAEs** (e.g., [36], [28]) employ random patch masking to train the model to reconstruct the masked patches. Top right: an attention map where each row represents the average attention score of all patches in a channel towards other channels and the [CLS] token (last column). Note that each patch primarily attends to its own channel (the diagonal) and the [CLS] token, resulting in minimal learned interactions between channels. This suggests that patch masking may not effectively promote cross-channel interactions in MCI. (B) **In contrast, Dynamic Channel-Patch Masking (ours)** encourages more interactions between patches across different channels by using both channel and patch masking. Also, *memory tokens* serve as long-term memory to help information aggregation across channels. Its attention pattern (bottom right) demonstrates a more uniform distribution across channels, indicating that each image patch can learn more meaningful interactions.

can vary in both the number and type of channels. These varying channel configurations arise from differences in sensor modalities, acquisition settings, or experimental conditions. Multi-Channel Imaging (MCI) models are designed to learn feature representations from heterogeneous channels whose type and number vary during both training and testing [6, 13]. This adaptability enhances the models’ robustness, allowing a single model to effectively handle di-

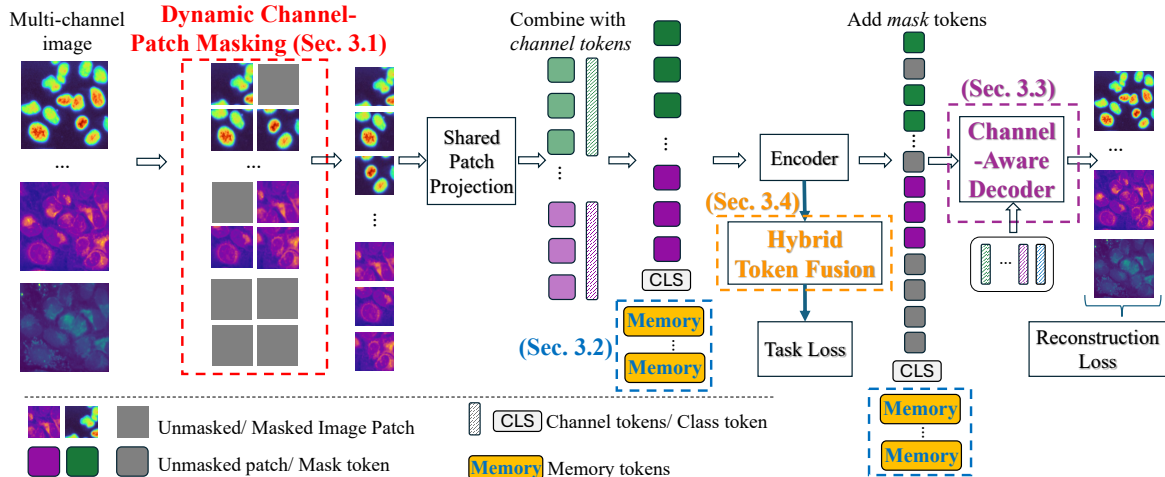


Figure 2. Our **ChA-MAEViT** approach enhances cross-channel learning via four key components: 1) **Dynamic Channel-Patch Masking**, which compels the model to reconstruct varying proportions of missing channels and patches, thus improving interactions across channels and robustness to the absence of some channels (Sec. 3.1). 2) **Memory Tokens**, which act as long-term memory to facilitate information sharing between channels (Sec. 3.2). 3) To reconstruct the masked patches and channels, we use a **Channel-Aware Decoder** that leverages channel tokens for image reconstruction, enhancing performance while minimizing computational costs (Sec. 3.3). 4) A **Hybrid Token Fusion** module, which combines fine-grained patch tokens with a global [CLS] token to improve feature representation (Sec. 3.4).

verse channel configurations, thereby reducing computational costs and minimizing the risk of overfitting [13].

Current MCI-Masked Autoencoder (MAE) models (*e.g.*, CA-MAE [28], MMEarth [36]) demonstrated promise in capturing local spatial structures by learning to reconstruct randomly masked patches in multi-channel images. These approaches assume that images exhibit significant redundancy across channels, enabling the reconstruction of masked patches using unmasked patches from similar channels. While this assumption works well for natural images, where color channels typically show strong correlations, it presents challenges in MCI scenarios. In these situations, complementary sensors (*e.g.*, multispectral and LiDAR) may capture distinct physical properties that have minimal feature overlap. As shown in Fig. 1(a), when using patch masking, the patch-to-channel attention concentrates on its own channel (the diagonal) and the [CLS] token (Fig. 1(a), top right). This indicates that prior MAE methods mainly focus on visible patches within the same channel, neglecting cross-channel feature interactions. This limitation restricts the model’s ability to learn useful features that require information from multiple channels.

To address this challenge, we introduce **Channel-Aware MAE** – multichannel **Vision Transformer** (ChA-MAEViT), which enhances cross-channel learning in MCI through four key improvements summarized in Fig. 2. First, we propose Dynamic Channel-Patch (DCP) Masking, which adaptively masks both patches and channels during training, compelling the model to reconstruct these missing patches and channels using the remaining patches (Fig. 2, left). DCP Masking adjusts the channel masking ratio to enhance feature learning and prepare the model

for partial channel availability during inference. Fig. 1(b) shows our approach redistributes the patch attention scores more evenly across channels, highlighting improved cross-channel interactions. However, in MCI reconstructing masked channels is challenging since each channel may encode unique features that are not easily inferred from others.

To enable the model to retain global information across all channels during reconstruction, we introduce the use of *memory tokens* in MCI (Fig. 2, middle). Inspired by register tokens [15], which are extra tokens added in the input to reduce artifacts in the feature maps of ViTs, these learnable embeddings serve as long-term memory to retain key cross-channel information in both the encoder and decoder. In addition, we use a hybrid token fusion module in the encoder to combine fine-grained patch tokens with the global class token for a richer representation (Fig. 2, middle).

Finally, we employ Channel-Aware Decoder that simultaneously processes patch tokens from all channels. Existing methods often rely on separate decoders for each channel [2, 28, 53], which do not scale well with many input channels. Our shared lightweight decoder utilizes channel tokens to provide channel-specific behavior and memory tokens to improve cross-channel feature reconstruction, enhancing performance while reducing computational costs.

Most of our experiments use both self-supervised (SSL) and supervised learning to boost performance, demonstrating a similar complimentary benefit from combining them observed in prior work (*e.g.*, [3, 14, 30, 51]). However, in the Supplementary, we also evaluate SSL by itself, where we demonstrate our approach still outperforms prior work.

The most relevant work to ours focuses on enhancing cross-channel interactions [19, 26, 52, 54]. However, these

approaches mainly use single-modality images, such as RGB, where channel similarities facilitate strong correlations. As noted earlier, this often does not generalize to the more complex MCI domain where channels convey varying information, *e.g.*, a robot sensor can contain LiDAR, RGB, and thermal camera. Thus, MCI requires a balance between preserving unique information in each channel and effectively modeling the complex relationships between channels. MCI models must also be robust to missing channels to support varying channel configurations [6, 13]. This means that cross-channel interaction should not only improve the overall representation but also involve learning useful redundancy across channels. ChA-MAEViT addresses these challenges by introducing DCP Masking to enhance cross-channel interaction while allowing the model to learn important channel-specific features, resulting in a more robust and higher-performing model.

Our key contributions are as follows:

- We explore ChA-MAEViT, an approach that integrates MAEs into MCI-ViTs for improved robustness that reports a gain of 3.0 – 21.5% across three diverse MCI datasets: CHAMMI [13], JUMP-CP [8], and So2Sat [56].
- We propose Dynamic Channel-Patch Masking that adaptively masks both channels and patches during training, compelling the model to reconstruct them from available patches to boost cross-channel feature interaction.
- We introduce Channel-Aware Decoder that uses channel tokens to reconstruct image patches more efficiently, thereby enhancing performance for downstream tasks.
- We utilize *memory tokens* and a Token Fusion module to enhance feature interaction and reconstruction. Memory tokens are learnable vectors that retain cross-channel information and aggregate channel-specific features, while the Token Fusion merges the [CLS] token with patch tokens to further improve feature representation.

2. Related Work

Many MCI methods do not use self-supervised objectives [5, 6, 39], but rather focus on aspects like diversity and robustness to missing channels. However, as noted in the introduction, self-supervised objectives like Masked Autoencoders (MAEs) can provide complementary information to further boost performance. MAEs themselves are often built for RGB images (*e.g.*, [23, 30, 50]) or those that are also strongly aligned like thermal images [53], which are based on assumptions of strong correlations between channels does not extend to many MCI images. Many methods in other domains followed suit, performing channel-wise masking on protein markers [45] or masked both of spatial and spectral channels [31, 49]. However, these methods rely on a fixed ratio of masked channels, which can be inadequate for the varying channel configurations found in MCI. In addition, prior work uses dual-branch architec-

tures that treats spatial and channel representations independently, limiting meaningful interactions between channels, especially when spatial alignment is not guaranteed. In contrast, we take a dynamic approach by randomly masking a variable number of channels each time. By combining both channel and patch-level masking within a single encoder, we achieve better feature interaction.

The work most similar to ours is CA-MAE [28], which randomly masks a fixed proportion of patches from all channels and employs distinct decoders for reconstruction. In contrast, ChA-MAEViT employs both channel and patch-level masking with a shared decoder, and memory tokens serve as long-term memory to facilitate feature interactions.

There are other types of self-supervised learning methods beyond MAEs that have been explored in other settings (*e.g.*, [1, 7, 10–12, 12, 17, 20, 21, 23, 38, 50, 55]). However, similar to MAEs, they often make assumptions that do not generalize to MCI images. For example, self-distillation methods (*e.g.*, SimSiam [12], BYOL [21], DINO [7]) process two different views through two encoders, and then map one view to the other using a predictor network. These methods often rely on complex augmentations designed for natural images to generate dual views, such as color jittering and Gaussian blur. These are less effective for MCI, where heterogeneous channels (*e.g.*, LiDAR, thermal, RGB) carry distinct physical properties. Such augmentations can distort critical features like depth or intensity, hindering the model’s ability to capture cross-channel dependencies essential for MCI. This makes masked modeling techniques attractive (*e.g.*, MAE [23], SimMim [50]), as they do not rely on augmentations that may be challenging to apply with more complex and varied images.

3. Channel-Aware Masked Autoencoders for Improved Cross-Channel Learning

Given a multi-channel image (MCI) denoted as X , which consists of various channels $c_i \in C$, our objective is to train a model M that takes X as input to generate representations and/or predictions. Following prior work [5, 6, 13, 39], we focus on the MCI setting where the model M is trained using all available channels C but tested with a subset of those channels $C_{\text{test}} \subseteq C$. We leave the exploration of supporting novel channels during inference to future work. Here, we describe the details of the four main components of our proposed framework, which is illustrated in Fig. 2.

3.1. Dynamic Channel-Patch Masking

As shown in Fig. 1(a), image patches in prior work seem to attend mostly to their own channels while neglecting the others, potentially missing rich interactions among channels. To mitigate this issue, we propose Dynamic Channel-Patch (DCP) Masking, which integrates both patch and channel-level masking strategies. We start creating image

patches (Suppl., Sec. 6), which results in n tokens per channel, each with d -dimensional embeddings, for c channels.

Our masking strategy consists of two components: *random patch masking* and *dynamic channel masking*. The first component, *random patch masking*, aims to generate a mask $\mathbf{p_mask} \in \{0, 1\}^{n \times c}$ that applies a fixed masking ratio r_p (e.g., 75%) to mask patches independently across each channel. Specifically, for each channel j , we first uniformly sample a set of $\lfloor n \cdot r_p \rfloor$ positions from the n available patch positions, denoted $S_j \subset \{1, 2, \dots, n\}$ with $|S_j| = \lfloor n \cdot r_p \rfloor$. We then mask these patches as follows:

$$\mathbf{p_mask}_{i,j} = \begin{cases} 1 & \text{if } i \in S_j, \\ 0 & \text{otherwise,} \end{cases} \quad (1)$$

where $\mathbf{p_mask}_{i,j} = 1$ indicates the patch at position i of channel j is masked, and $\mathbf{p_mask}_{i,j} = 0$ indicates unmasked. While all channels have the same number of masked patches, their specific locations vary per channel because they are independently sampled, as opposed to prior work that first generates the mask for one channel and then replicates it to all other channels [36, 49].

The second component, *dynamic channel masking*, aims to generate a mask $\mathbf{c_mask} \in \{0, 1\}^{n \times c}$ that adaptively mask out some channels. We start by uniformly sampling the number of channels to be masked, denoted as $k \sim \mathcal{U}\{0, 1, \dots, c - 1\}$. Then, we uniformly sample a set of k channels, denoted as $\mathcal{C}' \subset \{1, \dots, c\}$ with $|\mathcal{C}'| = k$, and mask these channels out as follows:

$$\mathbf{c_mask}_{*,j} = \begin{cases} 1^n & \text{if } j \in \mathcal{C}' \\ 0^n & \text{otherwise,} \end{cases} \quad (2)$$

for $\forall j \in [c]$. This masking approach is inspired by Hierarchical Channel Sampling (HCS) [5]. However, unlike HCS, which serves as a channel dropout technique that completely removes selected channels, our approach employs masked channels as supervisory signals, designating them as labels for the reconstruction process. This enables the model to directly learn inter-channel relationships by reconstructing the masked channels using the available ones, thus enhancing greater cross-channel feature interaction.

Finally, we integrate these two components for training images in our DCP Masking strategy by introducing hyperparameters $p_{\text{patch}}, p_{\text{channel}} \in (0, 1)$. These values divide the unit interval into three sections to randomly determine how to use one or the other type of mask, as follows:

$$\mathbf{mask} = \begin{cases} \mathbf{p_mask} & \text{if } s < p_{\text{patch}} \\ \mathbf{c_mask} & \text{if } p_{\text{patch}} \leq s < p_{\text{patch}} + p_{\text{channel}} \\ \mathbf{p_mask} \vee \mathbf{c_mask} & \text{otherwise} \end{cases} \quad (3)$$

where s is a selection value chosen uniformly at random. In practice, we found that optimizing the model with these two

masking strategies simultaneously can be difficult. Combining patch and channel masks into a single mask may lead to excessive information loss, making image reconstruction challenging. To address this, we adjust the hyperparameters to alternate between the two masking strategies separately. Specifically, setting $p_{\text{patch}} = p_{\text{channel}} = 0$ merges both patch and channel masks into a unified mask, and setting $p_{\text{patch}} = p_{\text{channel}} = 0.5$ allows the model to switch between patch and channel masks. We adopt these two configurations throughout our experiments. Refer to the Supplementary, Sec. 7 for the procedure of DCP Masking.

3.2. Memory Tokens

Reconstructing masked channels is challenging due to their inherent differences, since each channel encodes unique features not easily inferred from others, e.g., reconstructing LIDAR from RGB. Inspired by the concept of register tokens [15], which are used to reduce artifacts in the feature maps of ViTs, we introduce *memory tokens* for MCI (Fig. 2, middle). These memory tokens are learnable embeddings that serve as long-term memory, allowing for the storage of global information across all channels. During training, these tokens gather channel-specific features using cross-attention mechanisms, helping the model retain and propagate information across layers that might otherwise be lost due to masking. Additionally, these tokens assist in decoding image patches to facilitate the reconstruction process. During inference, memory tokens enable the model to retrieve stored context, effectively addressing the issue of missing channels. Similar to the [CLS] token, memory tokens are incorporated into the input during both training and inference. However, while the [CLS] token is utilized as the final representation, the memory tokens are excluded.

Formally, we prepend a set of l memory tokens $\{\mathbf{M}_i\}_{i \in [l]}$ into the input sequence, resulting in a sequence of $[\mathbf{t}_{\text{CLS}}; \mathbf{M}_1; \dots; \mathbf{M}_l; \mathbf{t}_{1,1}; \mathbf{t}_{2,1}; \dots; \mathbf{t}_{n,c}]$, where \mathbf{t}_{CLS} and $\mathbf{t}_{i,j}$ are the class token and patch token at i -th location of j -th channel, respectively. After masking some patches (Sec. 3.1), the remaining patches are fed into a transformer encoder. Following [5, 39], we encode spatial information via learnable positional embeddings and encode each channel’s unique characteristics with special *channel tokens*.

3.3. Channel-Aware Decoder

After processing the unmasked tokens with the encoder, we reconstruct the masked patches using the unmasked ones with a Channel-Aware Decoder. Unlike prior MCI-MAE methods that use separate decoders for each channel or modality [2, 28, 53], we employ a single decoder to process tokens from all channels simultaneously (Fig. 2, right). This scales better to the number of input channels (up to 18 in our experiments), while also boosting performance.

Let the output sequence from the encoder be

$[\hat{\mathbf{t}}_{\text{CLS}}; \hat{\mathbf{M}}_1; \dots; \hat{\mathbf{M}}_l; \hat{\mathbf{t}}_1; \hat{\mathbf{t}}_2; \dots; \hat{\mathbf{t}}_v]$, where v denotes the number of visible (*i.e.*, unmasked) patches fed into the encoder. This sequence is shorter than the original image patch length due to the missing masked patches. To reconstruct these masked patches, we utilize $u = (n \cdot c - v)$ mask tokens \mathbf{m}_i , where each mask token is a shared, learned vector representing the missing patch.

Incorporating Channel-Specific Information. To reconstruct channel-specific information, we combine patch tokens, whether visible ($\hat{\mathbf{t}}_i$) or masked (\mathbf{m}_i), with their corresponding *channel tokens*, which are also optimized by the encoder. We define $f(\cdot)$ as a function that returns the corresponding *channel token* for a given patch token. The input to our Channel-Aware Decoder is thus:

$$\hat{\mathbf{T}} = [\hat{\mathbf{t}}_{\text{CLS}}; \hat{\mathbf{M}}_1; \dots; \hat{\mathbf{M}}_l; \hat{\mathbf{t}}_1 + f(\hat{\mathbf{t}}_1); \hat{\mathbf{t}}_2 + f(\hat{\mathbf{t}}_2); \dots; \hat{\mathbf{t}}_v + f(\hat{\mathbf{t}}_v); \mathbf{m}_1 + f(\mathbf{m}_1), \dots, \mathbf{m}_u + f(\mathbf{m}_u)]$$

Incorporating channel tokens provides a more channel-specific context, which enhances the reconstruction process. Additionally, we incorporate learnable positional embeddings, which are shared with the encoder, to provide information about the position of each patch in the image.

Patch Reconstruction. We pass the token sequence $\hat{\mathbf{T}}$ into several Transformer Blocks, followed by a Decoder to reconstruct the pixels of each image patch. Let $\mathbf{T} \in \mathbb{R}^{(n \cdot c) \times d}$ represent the output of the patch tokens from the final Transformer Block. The Decoder is a linear layer $\mathbf{W}_{\text{decoder}} \in \mathbb{R}^{d \times p^2}$, where p is the image patch size. The pixel reconstruction of the i -th patch of the j -th channel, is computed as $\hat{\mathbf{x}}_{i,j} = (\mathbf{T}_{i,j} \cdot \mathbf{W}_{\text{decoder}}) \in \mathbb{R}^{p^2}$. We found that a lightweight decoder with just 1 – 2 Transformer Blocks is sufficient, aligning with findings from prior work [23, 30].

Reconstruction Loss. We use standard $L2$ loss on the image pixel, and the Fourier space $L1$ loss introduced in [28], both computed only on the masked patches. Let $P = \sum_{i=1}^n \sum_{j=1}^c \text{mask}_{i,j}$ be the number of masked patches of the input image. Given $\mathbf{x}_{i,j}, \hat{\mathbf{x}}_{i,j} \in \mathbb{R}^{p^2}$, the original pixels of patch i in channel j , and its reconstruction, respectively, the reconstruction loss is as follows:

$$\begin{aligned} \mathcal{L}_{\text{pixel}} &= \frac{1}{P} \sum_{i=1}^n \sum_{j=1}^c \text{mask}_{i,j} \cdot L_2(\mathbf{x}_{i,j}, \hat{\mathbf{x}}_{i,j}) \\ \mathcal{L}_{\text{fourier}} &= \frac{1}{P} \sum_{i=1}^n \sum_{j=1}^c \text{mask}_{i,j} \cdot L_1(|\mathcal{F}(\mathbf{x}_{i,j})|, |\mathcal{F}(\hat{\mathbf{x}}_{i,j})|) \\ \mathcal{L}_{\text{recon}} &= (1 - \lambda_f) \cdot \mathcal{L}_{\text{pixel}} + \lambda_f \cdot \mathcal{L}_{\text{fourier}}, \end{aligned} \quad (4)$$

where \mathcal{F} is the Fast Fourier Transform. Following [28], we set to a fixed $\lambda_f = 0.01$.

3.4. Hybrid Token Fusion

Prior work either utilizes the [CLS] token [15, 37] or average pooling of patch tokens [28, 30] for downstream tasks. We found that incorporating both the [CLS] token and the

patch tokens in our framework yields better performance (Fig. 2, middle). Given the output sequence from the encoder, we use a learnable query vector $\mathbf{q}_{\text{patch}}$ to interact with the patch tokens. The query attends to the patch tokens through cross-attention, and then combined with the [CLS] token to generate a fused representation:

$$f_{\text{fusion}} = \hat{\mathbf{t}}_{\text{CLS}} \odot \sigma(\text{CrossAttention}(\mathbf{q}_{\text{patch}}, \mathbf{T}_p)), \quad (5)$$

where $\mathbf{T}_p = [\hat{\mathbf{t}}_1; \hat{\mathbf{t}}_2; \dots; \hat{\mathbf{t}}_v]$, \odot represents the elementwise product, and σ the sigmoid function. The fused representation, f_{fusion} , integrates global context from the [CLS] token while also being refined by detailed spatial information from the patch tokens. We then use a multi-layer perceptron (MLP) with GELU activation [24] to enhance the fusion representation and tailor it for downstream tasks:

$$f_{\text{final}} = \text{Linear}(\text{GELU}(\text{Linear}(f_{\text{fusion}}))) \quad (6)$$

Training Objective. The output of Eq. (6) is then used to compute the task loss, *e.g.*, cross-entropy for classification. Our final loss consists of three components: the primary loss for the specific task $\mathcal{L}_{\text{task}}$, regularization term \mathcal{L}_{d} , and reconstruction loss $\mathcal{L}_{\text{recon}}$ (Eq. (4)) as follows:

$$\mathcal{L}_{\text{final}} = (1 - \lambda_{\text{recon}}) \cdot (\mathcal{L}_{\text{task}} + \lambda_{\text{d}} \cdot \mathcal{L}_{\text{d}}) + \lambda_{\text{recon}} \cdot \mathcal{L}_{\text{recon}}, \quad (7)$$

where λ_{d} is to balance the task loss and the regularization term, and λ_{recon} is to balance the reconstruction loss with other losses. For regularization \mathcal{L}_{d} , we use the losses introduced in [39], in which Channel Diversification Loss applies to the channel tokens, and Token Diversification Loss applies to the patch tokens to encourage diversity learning. We set λ_{d} as recommended by [39] for each dataset, and a fixed $\lambda_{\text{recon}} = 0.99$ for all the experiments.

4. Experiments

4.1. Datasets

CHAMMI [13] consists of varying-channel images sourced from three datasets: WTC-11 (3 channels), the Human Protein Atlas (HPA, 4 channels), and the Cell Painting Gallery (CP, 5 channels). Together, these three datasets contain a total of 220K microscopy images, in which, 100K images are designated for training, while the remainder is used for testing across various domain generalization tasks. **JUMP-CP** [8] is a cellular imaging dataset that includes microscopy images and profiles of cells subjected to both chemical and genetic perturbations. We use compound perturbation plate BR00116991, which contains 127K training images, 45K validation images, and 45K test images, across 161 classes. Each image has 8 channels, consisting of 5 fluorescence channels and 3 brightfield channels.

So2Sat [56] includes synthetic aperture radar and multi-spectral optical image patches collected from remote sensing satellites. Each image contains 18 channels: 8 channels

Model	CHAMMI [13]	JUMP-CP [8]		So2Sat [56]	
	Avg score	Full	Partial	Full	Partial
HyperNetViT [22]	56.08±0.41	47.07±0.47	42.43±0.65	60.73±0.24	41.88±0.85
DepthwiseViT [13]	61.80±0.43	49.86±0.45	44.98±0.71	60.41±0.22	43.41±1.10
TemplateMixingViT [40, 41, 44]	58.16±0.42	52.48±0.27	43.85±0.73	55.86±0.10	37.28±0.34
CA-MAE [28] + Supervised loss	59.15±0.28	69.54±0.12	20.93±0.25	64.21±0.41	15.75±0.83
ChAda-ViT [6]	63.93±0.42	65.03±0.98	42.15±2.33	56.98±0.46	12.38±2.03
ChannelViT [5]	64.97±0.58	67.51±0.35	56.49±0.53	61.03±0.17	46.16±0.40
DiChaViT [39]	69.77±0.44	69.19±0.47	57.98±0.41	63.36±0.11	47.76±0.23
ChA-MAEViT (ours)	74.63±0.54	90.73±0.14	68.15±0.10	67.44±0.38	52.11±0.49

Table 1. **Comparison of channel adaptive models.** We report the mean accuracy with standard deviation on the test set of three runs. “Full” refers to inference on all channels, while “Partial” means inference on a subset of channels. ChA-MAEViT outperforms other baselines consistently across three datasets, by 5.0% on CHAMMI, 10.0 – 21.5% on JUMP-CP, and 3.0 – 4.5% on So2Sat. Note: all models contain the same number of parameters, except CA-MAE due to its separate decoders (*e.g.*, 4X parameters on So2Sat).

from Sentinel-1, and the rest from Sentinel-2. The dataset comprises 17 classes that represent different climate zones. We use the city-split version, which consists of 352K training images, 24K validation images, and 24K test images.

4.2. Experimental Setup

Baseline methods. We compare to the following methods:

- **DepthwiseViT** [13] processes each input channel through a depthwise convolution layer, averages the filtered features, and feeds them into a ViT backbone.
- **TemplateMixingViT** [40, 41, 44] learns channel weights via shared parameter templates, forming a patch projection layer for a ViT backbone.
- **HyperNetViT** [22] uses a neural network to generate channel-specific weights, concatenating them into a patch projection layer for a ViT backbone.
- **CA-MAE** [28] applies MAE to multi-channel data in SSL settings. We add task loss to adapt this baseline.
- **ChAda-ViT** [6] employs a shared projection for channel-wise feature extraction, combining the tokens with positional and channel embeddings for ViT processing.
- **ChannelViT** [5] Similar to ChAda-ViT, while incorporating Hierarchical Channel Sampling during training.
- **DiChaViT** [39] improves ChannelViT with regularization terms and a diverse channel sampling technique.

Additionally, we investigate the effect of combining the best supervised baseline, DiChaViT, with the following SSL to evaluate the importance of incorporating self-supervision: MAE [23], SimCLR [10, 11], SimSiam [12], iBOT [55], and DINOv2 [38]. More details in Suppl., Sec. 8.

Implementation details. For most of the baseline models, such as HyperNetViT, ChannelViT, ChAda-ViT, and DiChaViT, we utilize the implementation from [39]¹. For iBOT and DINOv2, we adapt the implementation from

[38]². All baselines employ a ViT small with 21M parameters as the backbone. In our method, we remove one transformer block from the encoder to accommodate the decoder, ensuring that our approach maintains the same number of parameters as the baselines. We use the AdamW optimizer [35] to train the models, minimizing cross-entropy loss on the JUMP-CP and So2Sat, and proxy loss [13] on CHAMMI. Refer to Supplementary Sec. 9 for details.

Metrics. We evaluated the methods by calculating their top-1 classification accuracy on the So2Sat [56] and JUMP-CP [8]. For CHAMMI [13], we utilized the evaluation code provided by the authors³. Following [39], we report the average F1 scores across the WTC-11 and HPA.

4.3. Results

Tab. 1 compares ChA-MAEViT with different MCI-ViTs. ChA-MAEViT significantly outperforms the baseline models by an average of 10.0% across three datasets. Specifically, ChA-MAEViT exceeds the state-of-the-art model DiChaViT by 5.0% on CHAMMI, a channel-adaptive benchmark. For JUMP-CP and So2Sat, we conducted evaluations in both *Full* (using all channels) and *Partial* (using subsets of channels) settings. In the full setting, our model surpasses the next best models by 21.5% and 3.0%, respectively. Additionally, ChA-MAEViT demonstrates its robustness in the partial settings, where we test JUMP-CP using five fluorescence channels and So2Sat using eight Sentinel-1 channels, showing improvement of 10.0% and 4.5% points respectively over prior work.

Tab. 2 presents the impact of integrating various SSL methods with the top-performing supervised approach, DiChaViT [39]. In the last row, we train DiChaViT to reconstruct the masked patches using only our DCP Masking, without incorporating *memory tokens*, Hybrid Token

¹https://github.com/chaudatascience/diverse_channel_vit

²<https://github.com/facebookresearch/dinov2>

³<https://github.com/broadinstitute/MorphEm>

DiChaViT [39] +	CHAMMI	JUMP-CP		So2Sat	
	Avg score	Full	Partial	Full	Partial
SimCLR [10, 11]	70.72	67.67	57.92	<u>64.93</u>	<u>49.37</u>
SimSiam [12]	70.66	69.43	58.58	64.13	48.85
iBOT [55]	70.76	68.87	57.81	63.12	47.80
DINOv2 [38]	70.06	66.91	56.18	63.53	49.23
MAE [23]	<u>70.89</u>	<u>78.33</u>	<u>63.28</u>	62.92	47.85
DCP Masking	71.52	84.02	65.72	66.03	50.55

Table 2. Comparison of SSL methods when combined with the best supervised baseline DiChaViT [39]. The last row shows the combination of DiChaViT with Dynamic Channel-Patch Masking. Incorporating SSL in DiChaViT results in improvements. Best result with our masking strategy. **Boldfaces** and underlines indicates best and second best numbers, respectively.

Fusion, or Channel-Aware Decoder. While the combination with MAE gives the highest performance, DCP still significantly outperforms the best SSL-enhanced variant by 0.6 – 5.6% across three datasets. The performance gap highlights the effectiveness of DCP, which substantially exceeds the improvements gained from solely combining with SSL objectives. The lower performance of some SSL methods, such as SimCLR and DINOv2, may be due to their reliance on augmentation pipelines designed for RGB images, which are less effective for heterogeneous channels in multi-channel images. In contrast, our MAE-based approach does not rely on heavy augmentations. Additionally, by only processing the unmasked patches, our method achieves significantly faster runtime compared to other SSL methods, *e.g.*, 5X faster than DINOv2, making it both performant and computationally efficient for MCI tasks.

Tab. 3 evaluates ChA-MAEViT and the best baseline DiChaViT [39] when tested on varying numbers of channels of JUMP-CP. We train the model using all eight channels and assess performance after removing channels. The average accuracy is calculated across all possible combinations, *e.g.*, testing with seven channels, as shown in column “7,” the results of $C_8^7 = 8$ combinations are averaged (Supplementary Tab. 7 for details). ChA-MAEViT demonstrates enhanced robustness, particularly when some channels are missing during inference.

Comparing masking strategies. Tab. 4 compares various masking strategies applied to ChA-MAEViT. For fixed ratio approaches, we test several ratios (*e.g.*, 50%, 75%) and report the best results based on the validation set. We observe that DCP Masking consistently outperforms others, achieving the highest scores in both Full and Partial settings. Notably, while random patch masking is effective in Full, it experiences a significant performance drop in Partial settings. In contrast, dynamic channel masking methods adapted from [5, 39] provide better adaptability for partial settings, and our DCP approach improves even

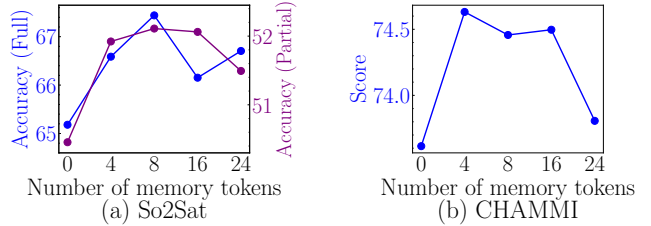


Figure 3. Numbers of memory tokens. (a) So2Sat. Using memory tokens improves performance in both Full (blue line) and Partial (purple line) settings, with the best accuracy achieved with 8 memory tokens. (b) CHAMMI. A similar trend occurs, with the best performance at 4 memory tokens. However, using more memory tokens (*e.g.*, 24) may reduce the effectiveness of the model.

more. In addition, we analyze two variants of DCP: Combination and Alternate. The DCP Combination unifies both patch and channel masks, while the DCP Alternate switches between the two for each training iteration. Both variants outperform traditional patch- and channel-based masking methods, highlighting the effectiveness of joint channel-patch masking. Refer to Supplementary, Sec. 10.4 for more analysis, such as the impact of varying *random patch masking ratios* r_p in DCP Combination, proportions of *channel-* and *patch-level* masking in DCP Alternate, and patch masking strategies in DCP.

4.4. Model ablations and sensitivity analysis

Impact of Memory tokens. Fig. 3 shows the accuracy achieved by varying the numbers of *memory tokens* on So2Sat and CHAMMI. For both datasets, memory tokens enhance performance but beyond a certain point yield diminishing returns. This suggests that while memory tokens can improve performance, excessive reliance on them may negatively impact the interaction of patch features. Supplementary, Sec. 10.5 reports analysis of attention patterns of memory tokens and their impact on the reconstruction loss.

Token pooling strategies. Tab. 5 compares the performance of various token pooling strategies on CHAMMI and So2Sat. In general, combining the [CLS] token with the average of the patch tokens gets better performance than either alone. Hybrid Token Fusion further improves performance, consistently outperforms others across all settings.

Lambda for reconstruction loss. Fig. 4 analyzes the effect of the reconstruction loss weight λ_{recon} (Eq. (7)) on model performance. Similar to prior work [30, 51], a large value of $\mathcal{L}_{\text{recon}}$, such as 0.99, gives the best results. However, performance drops significantly using just the MAE loss (*i.e.*, $\lambda_{\text{recon}} = 1$), noting the contributions of both losses.

Channel-Aware Decoder analysis. Fig. 5 shows Channel-Aware Decoder in ChA-MAEViT outperforms both Separate Decoders [28] and Shared Decoder W/out Channel Tokens by 1.1 – 3.2% across three datasets in full and partial settings. Channel-Aware Decoder is also more efficient than

Method	Number of channels at inference							
	8	7	6	5	4	3	2	1
DiChaViT [39]	69.19	61.91±9.3	54.49±12.4	46.35±13.4	38.00±12.4	30.09±9.3	23.97±4.9	20.90±1.6
ChA-MAEViT (ours)	90.73	83.36±8.3	74.55±11.7	63.46±13.8	50.85±13.9	38.13±11.2	27.62±6.4	21.59±2.1

Table 3. **Performance on varying channel configurations during inference.** Columns report the *mean ± std* for all channel combinations on JUMP-CP [8], e.g. “7” indicates testing on 7 out of 8 channels ($C_8^7 = 8$ combinations). ChA-MAEViT consistently shows improved robustness with missing channels at test time. The reported variance results from either the presence or absence of a channel. Refer to Table 7 in the Supplementary for model variance report.

Mask Strategy	CHAMMI [13]	JUMP-CP [8]		So2Sat [56]	
	Avg score	Full	Partial	Full	Partial
Random Patch (fixed ratio) (e.g., [2, 18, 27, 28, 30, 36])	70.51	88.01	52.33	64.50	28.70
Random Patch (dynamic)	68.23	85.54	55.86	64.84	31.92
Channel (fixed ratio) [53]	47.97	73.00	65.25	65.22	38.59
Hierarchical Channel Sampling (dynamic, adapted [5])	69.86	83.71	67.75	65.20	48.77
Diverse Channel Sampling (dynamic, adapted [39])	71.57	84.69	67.86	65.49	51.05
Channel + Patch (fixed ratio) [49]	48.46	69.41	62.19	62.20	32.18
DCP Combination ($p_{\text{channel}} = p_{\text{patch}} = 0$) (ours)	73.75	85.95	68.36	67.44	52.11
DCP Alternate ($p_{\text{channel}} = p_{\text{patch}} = 0.5$) (ours)	74.63	90.73	68.15	66.47	50.69

Table 4. **Comparison of Mask strategies in MCI when using with ChA-MAEViT.** While *Random Patch* and *Channel Sampling* perform similarly on Full channels, *Random Patch* experiences a significant drop in Partial channel settings. Dynamic Channel-Patch (DCP) Masking demonstrates its effectiveness in both Full and Partial channel settings, outperforming all strategies across three datasets.

Token Pooling Method	CHAMMI	So2Sat	
		Full	Partial
Avg Patch tokens	71.41	64.86	51.87
[CLS] token	73.84	65.48	51.40
[CLS] + Avg Patch tokens	73.96	66.23	49.45
Hybrid Token Fusion (ours)	74.63	67.44	52.11

Table 5. **Comparison of token pooling methods.** Hybrid Token Fusion achieves the best performance, demonstrating the benefit of leveraging both global and local token representations.

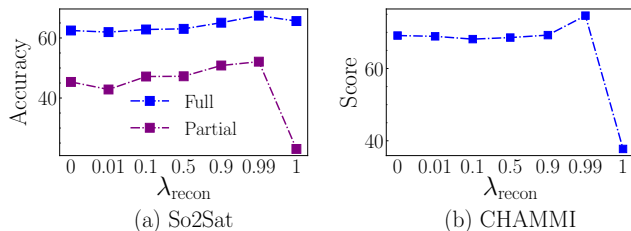


Figure 4. **Impact of reconstruction lambda λ_{recon} (Eq. (7)).** $\lambda_{\text{recon}} = 0$ means without the reconstruction loss, while $\lambda_{\text{recon}} = 1$ indicates only using the reconstruction loss. For $\lambda_{\text{recon}} = 1$ on So2Sat, we run linear probing. $\lambda_{\text{recon}} = 0.99$ works best for ChA-MAEViT on both datasets.

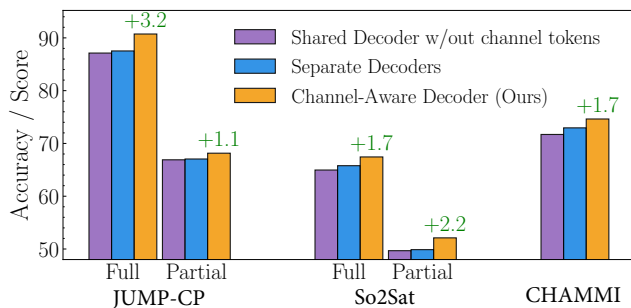


Figure 5. **Comparison of Channel-Aware Decoder with Separate Decoders [28] and Shared Decoder W/out Channel Tokens** when using with ChA-MAEViT. Our method outperforms the best baseline by 1.1 – 3.2% on both channel settings across three datasets.

Separate Decoders, e.g., 18X fewer parameters on So2Sat.

5. Conclusion

In this paper, we introduce ChA-MAEViT, a novel MAE-based method to enhance feature learning in Multi-Channel Imaging (MCI) ViTs. First, we introduce Dynamic Channel-Patch Masking, in which we adaptively mask both image patches and channels and train the model to reconstruct the masked patches. Additionally, we incorpo-

rate *memory tokens* to preserve global context across channels and Hybrid Token Fusion module to combine features from local patch tokens and global class tokens. Furthermore, we propose Channel-Aware Decoder to efficiently reconstruct channel-specific details. Experiments conducted on the CHAMMI, JUMP-CP, and So2Sat datasets demonstrate that ChA-MAEViT outperforms prior MCI-ViT by 3.0 – 21.5%, highlighting the significance of enhanced cross-channel interactions. These advancements provide a flexible and effective framework for addressing challenges in MCI, paving the way for future improvements in MCI-ViT research.

Acknowledgments. This study was supported, in part, by the National Science Foundation under NSF-DBI awards 2134695 and 2134696. Any opinions, findings, and conclusions or recommendations expressed in this material are those of the author(s) and do not necessarily reflect the views of the supporting agencies.

References

- [1] Mahmoud Assran, Mathilde Caron, Ishan Misra, Piotr Bojanowski, Florian Bordes, Pascal Vincent, Armand Joulin, Mike Rabbat, and Nicolas Ballas. Masked siamese networks for label-efficient learning. In *European Conference on Computer Vision*, pages 456–473. Springer, 2022. 3
- [2] Roman Bachmann, David Mizrahi, Andrei Atanov, and Amir Zamir. Multimaes: Multi-modal multi-task masked autoencoders. In *European Conference on Computer Vision*, pages 348–367. Springer, 2022. 2, 4, 8
- [3] Junwen Bai, Bo Li, Yu Zhang, Ankur Bapna, Nikhil Sidhartha, Khe Chai Sim, and Tara N Sainath. Joint unsupervised and supervised training for multilingual asr. In *ICASSP 2022-2022 IEEE International Conference on Acoustics, Speech and Signal Processing (ICASSP)*, pages 6402–6406. IEEE, 2022. 2
- [4] Hangbo Bao, Li Dong, Songhao Piao, and Furu Wei. BEit: BERT pre-training of image transformers. In *International Conference on Learning Representations*, 2022. 1
- [5] Yujia Bao, Srinivasan Sivanandan, and Theofanis Karaletsos. Channel vision transformers: An image is worth $1 \times 16 \times 16$ words. In *The Twelfth International Conference on Learning Representations*, 2024. 3, 4, 6, 7, 8, 2, 5
- [6] Nicolas Bourriez, Ihab Bendidi, Cohen Ethan, Gabriel Watkinson, Maxime Sanchez, Guillaume Bollot, and Auguste Genovesio. Chada-vit : Channel adaptive attention for joint representation learning of heterogeneous microscopy images. In *The IEEE Conference on Computer Vision and Pattern Recognition (CVPR)*, 2024. 1, 3, 6
- [7] Mathilde Caron, Hugo Touvron, Ishan Misra, Hervé Jégou, Julien Mairal, Piotr Bojanowski, and Armand Joulin. Emerging properties in self-supervised vision transformers. In *Proceedings of the IEEE/CVF international conference on computer vision*, pages 9650–9660, 2021. 3
- [8] Srinivas Niranj Chandrasekaran, Beth A. Cimini, Amy Goodale, Lisa Miller, Maria Kost-Alimova, Nasim Jamali, John Doench, Briana Fritchman, Adam Skepner, Michelle Melanson, John Arevalo, Juan C. Caicedo, Daniel Kuhn, Desiree Hernandez, Jim Berstler, Hamdah Shafqat-Abbasi, David Root, Sussane Swalley, Shantanu Singh, and Anne E. Carpenter. Three million images and morphological profiles of cells treated with matched chemical and genetic perturbations. *bioRxiv*, 2022. 3, 5, 6, 8, 2, 4
- [9] Min Chen, Aaron Carass, Amod Jog, Junghoon Lee, Snehashis Roy, and Jerry L Prince. Cross contrast multi-channel image registration using image synthesis for mr brain images. *Medical image analysis*, 36:2–14, 2017. 1
- [10] Ting Chen, Simon Kornblith, Mohammad Norouzi, and Geoffrey Hinton. A simple framework for contrastive learning of visual representations. In *International conference on machine learning*, pages 1597–1607. PMLR, 2020. 3, 6, 7, 1
- [11] Ting Chen, Simon Kornblith, Kevin Swersky, Mohammad Norouzi, and Geoffrey E Hinton. Big self-supervised models are strong semi-supervised learners. *Advances in neural information processing systems*, 33:22243–22255, 2020. 6, 7, 1
- [12] Xinlei Chen and Kaiming He. Exploring simple siamese representation learning. In *Proceedings of the IEEE/CVF conference on computer vision and pattern recognition*, pages 15750–15758, 2021. 3, 6, 7, 1
- [13] Zitong Chen, Chau Pham, Siqi Wang, Michael Doron, Nikita Moshkov, Bryan A. Plummer, and Juan C Caicedo. CHAMMI: A benchmark for channel-adaptive models in microscopy imaging. In *Thirty-seventh Conference on Neural Information Processing Systems Datasets and Benchmarks Track*, 2023. 1, 2, 3, 5, 6, 8
- [14] Yong Cheng, Wei Wang, Lu Jiang, and Wolfgang Macherey. Self-supervised and supervised joint training for resource-rich machine translation. In *International Conference on Machine Learning*, pages 1825–1835. PMLR, 2021. 2
- [15] Timothée Darcet, Maxime Oquab, Julien Mairal, and Piotr Bojanowski. Vision transformers need registers. In *The Twelfth International Conference on Learning Representations*, 2024. 2, 4, 5
- [16] Gianluca Donato and Serge Belongie. Approximate thin plate spline mappings. In *Computer Vision—ECCV 2002: 7th European Conference on Computer Vision Copenhagen, Denmark, May 28–31, 2002 Proceedings, Part III 7*, pages 21–31. Springer, 2002. 2
- [17] Debidatta Dwibedi, Yusuf Aytar, Jonathan Tompson, Pierre Sermanet, and Andrew Zisserman. With a little help from my friends: Nearest-neighbor contrastive learning of visual representations. In *Proceedings of the IEEE/CVF International Conference on Computer Vision*, pages 9588–9597, 2021. 3
- [18] Alexandre Eymaël, Renaud Vandeghen, Anthony Cioppa, Silvio Giancola, Bernard Ghanem, and Marc Van Droogenbroeck. Efficient image pre-training with siamese cropped masked autoencoders. In *European Conference on Computer Vision*, pages 348–366. Springer, 2024. 8
- [19] Yu Gao, Xintong Han, Xun Wang, Weilin Huang, and Matthew Scott. Channel interaction networks for fine-grained image categorization. In *Proceedings of the AAAI conference on artificial intelligence*, pages 10818–10825, 2020. 2

- [20] Jonas Geiping, Quentin Garrido, Pierre Fernandez, Amir Bar, Hamed Pirsiavash, Yann LeCun, and Micah Goldblum. A cookbook of self-supervised learning. *arXiv preprint arXiv:2304.12210*, 2023. 3
- [21] Jean-Bastien Grill, Florian Strub, Florent Alché, Corentin Tallec, Pierre Richemond, Elena Buchatskaya, Carl Doersch, Bernardo Avila Pires, Zhaohan Guo, Mohammad Gheshlaghi Azar, et al. Bootstrap your own latent—a new approach to self-supervised learning. *Advances in neural information processing systems*, 33:21271–21284, 2020. 3
- [22] David Ha, Andrew Dai, and Quoc Le. Hypernetworks. In *International Conference on Learning Representations (ICLR)*, 2016. 6, 3
- [23] Kaiming He, Xinlei Chen, Saining Xie, Yanghao Li, Piotr Dollár, and Ross Girshick. Masked autoencoders are scalable vision learners. In *Proceedings of the IEEE/CVF conference on computer vision and pattern recognition*, pages 16000–16009, 2022. 3, 5, 6, 7, 1
- [24] Dan Hendrycks and Kevin Gimpel. Gaussian error linear units (gelus). *arXiv preprint arXiv:1606.08415*, 2016. 5
- [25] Andrew G Howard, Menglong Zhu, Bo Chen, Dmitry Kalenichenko, Weijun Wang, Tobias Weyand, Marco Andreetto, and Hartwig Adam. Mobilenets: Efficient convolutional neural networks for mobile vision applications. *arXiv preprint arXiv:1704.04861*, 2017. 1
- [26] Jie Hu, Li Shen, and Gang Sun. Squeeze-and-excitation networks. In *Proceedings of the IEEE conference on computer vision and pattern recognition*, pages 7132–7141, 2018. 2
- [27] Kian Kenyon-Dean, Zitong Jerry Wang, John Urbanik, Konstantin Donhauser, Jason Hartford, Saber Saberian, Nil Sahin, Ihab Bendi, Safiye Celik, Juan Sebastián Rodríguez Vera, Marta Fay, Imran S Haque, and Oren Kraus. Vitaly consistent: Scaling biological representation learning for cell microscopy, 2025. 8
- [28] Oren Kraus, Kian Kenyon-Dean, Saber Saberian, Maryam Fallah, Peter McLean, Jess Leung, Vasudev Sharma, Ayla Khan, Jia Balakrishnan, Safiye Celik, et al. Masked autoencoders for microscopy are scalable learners of cellular biology. In *Proceedings of the IEEE/CVF Conference on Computer Vision and Pattern Recognition*, pages 11757–11768, 2024. 1, 2, 3, 4, 5, 6, 7, 8
- [29] Xuelei Li, Liangkui Ding, Li Wang, and Fang Cao. Fpga accelerates deep residual learning for image recognition. In *2017 IEEE 2nd Information Technology, Networking, Electronic and Automation Control Conference (ITNEC)*, pages 837–840. IEEE, 2017. 1
- [30] Feng Liang, Yangguang Li, and Diana Marculescu. Supmae: Supervised masked autoencoders are efficient vision learners. *arXiv preprint arXiv:2205.14540*, 2022. 2, 3, 5, 7, 8
- [31] Junyan Lin, Feng Gao, Xiaochen Shi, Junyu Dong, and Qian Du. Ss-mae: Spatial–spectral masked autoencoder for multisource remote sensing image classification. *IEEE Transactions on Geoscience and Remote Sensing*, 61:1–14, 2023. 3
- [32] Yue Liu, Yunjie Tian, Yuzhong Zhao, Hongtian Yu, Lingxi Xie, Yaowei Wang, Qixiang Ye, Jianbin Jiao, and Yunfan Liu. Vmamba: Visual state space model. *Advances in neural information processing systems*, 37:103031–103063, 2025. 1
- [33] Ze Liu, Yutong Lin, Yue Cao, Han Hu, Yixuan Wei, Zheng Zhang, Stephen Lin, and Baining Guo. Swin transformer: Hierarchical vision transformer using shifted windows. In *Proceedings of the IEEE/CVF international conference on computer vision*, pages 10012–10022, 2021.
- [34] Zhuang Liu, Hanzi Mao, Chao-Yuan Wu, Christoph Feichtenhofer, Trevor Darrell, and Saining Xie. A convnet for the 2020s. In *IEEE/CVF Conference on Computer Vision and Pattern Recognition (CVPR)*, 2022. 1
- [35] Ilya Loshchilov and Frank Hutter. Decoupled weight decay regularization. In *International Conference on Learning Representations*, 2019. 6
- [36] Vishal Nedungadi, Ankit Kariryaa, Stefan Oehmcke, Serge Belongie, Christian Igel, and Nico Lang. Mmearth: Exploring multi-modal pretext tasks for geospatial representation learning. In *European Conference on Computer Vision*, pages 164–182. Springer, 2024. 1, 2, 4, 8
- [37] Maxime Oquab, Timothée Darcet, Theo Moutakanni, Huy V. Vo, Marc Szafraniec, Vasil Khalidov, Pierre Fernandez, Daniel Haziza, Francisco Massa, Alaaeldin El-Nouby, Russell Howes, Po-Yao Huang, Hu Xu, Vasu Sharma, Shang-Wen Li, Wojciech Galuba, Mike Rabbat, Mido Assran, Nicolas Ballas, Gabriel Synnaeve, Ishan Misra, Herve Jegou, Julien Mairal, Patrick Labatut, Armand Joulin, and Piotr Bojanowski. Dinov2: Learning robust visual features without supervision, 2023. 5
- [38] Maxime Oquab, Timothée Darcet, Théo Moutakanni, Huy V. Vo, Marc Szafraniec, Vasil Khalidov, Pierre Fernandez, Daniel HAZIZA, Francisco Massa, Alaaeldin El-Nouby, Mido Assran, Nicolas Ballas, Wojciech Galuba, Russell Howes, Po-Yao Huang, Shang-Wen Li, Ishan Misra, Michael Rabbat, Vasu Sharma, Gabriel Synnaeve, Hu Xu, Herve Jegou, Julien Mairal, Patrick Labatut, Armand Joulin, and Piotr Bojanowski. DINOv2: Learning robust visual features without supervision. *Transactions on Machine Learning Research*, 2024. Featured Certification. 3, 6, 7, 1, 2
- [39] Chau Pham and Bryan A. Plummer. Enhancing feature diversity boosts channel-adaptive vision transformers. In *Advances in Neural Information Processing Systems (NeurIPS)*, 2024. 3, 4, 5, 6, 7, 8, 1, 2
- [40] Chau Pham, Piotr Teterwak, Soren Nelson, and Bryan A. Plummer. Mixturegrowth: Growing neural networks by recombining learned parameters. In *IEEE Winter Conference on Applications of Computer Vision (WACV)*, 2024. 6, 3
- [41] Bryan A. Plummer, Nikoli Dryden, Julius Frost, Torsten Hoefler, and Kate Saenko. Neural parameter allocation search. In *International Conference on Learning Representations (ICLR)*, 2022. 6, 3
- [42] Chaitanya Ryali, Yuan-Ting Hu, Daniel Bolya, Chen Wei, Haoqi Fan, Po-Yao Huang, Vaibhav Aggarwal, Arkabandhu Chowdhury, Omid Poursaeed, Judy Hoffman, et al. Hiera: A hierarchical vision transformer without the bells-and-whistles. *arXiv preprint arXiv:2306.00989*, 2023. 1
- [43] Alexandre Sablayrolles, Matthijs Douze, Cordelia Schmid, and Hervé Jégou. Spreading vectors for similarity search. In *International Conference on Learning Representations*, 2019. 2

- [44] Pedro Savarese and Michael Maire. Learning implicitly recurrent CNNs through parameter sharing. In *International Conference on Learning Representations (ICLR)*, 2019. 6, 3
- [45] Zachary Sims, Gordon B Mills, and Young Hwan Chang. Mim-cycif: masked imaging modeling for enhancing cyclic immunofluorescence (cycif) with panel reduction and imputation. *bioRxiv*, 2023. 3
- [46] Christian Szegedy, Wei Liu, Yangqing Jia, Pierre Sermanet, and Scott Reed. Dragomiranguelov, dimitru erhan, vincent vanhoucke, and andrew rabinovich. 2015. going deeper with convolutions. In *Proceedings of the IEEE conference on computer vision and pattern recognition*, pages 1–9, 2015. 1
- [47] Mingxing Tan and Quoc Le. Efficientnet: Rethinking model scaling for convolutional neural networks. In *International conference on machine learning*, pages 6105–6114. PMLR, 2019. 1
- [48] Eu Wern Teh, Terrance DeVries, and Graham W Taylor. Proxynca++: Revisiting and revitalizing proxy neighborhood component analysis. In *Computer Vision—ECCV 2020: 16th European Conference, Glasgow, UK, August 23–28, 2020, Proceedings, Part XXIV 16*, pages 448–464. Springer, 2020. 2
- [49] Yue Wang, Ming Wen, Hailiang Zhang, Jinyu Sun, Qiong Yang, Zhimin Zhang, and Hongmei Lu. Hsimae: A unified masked autoencoder with large-scale pre-training for hyperspectral image classification. *IEEE Journal of Selected Topics in Applied Earth Observations and Remote Sensing*, 2024. 3, 4, 8
- [50] Zhenda Xie, Zheng Zhang, Yue Cao, Yutong Lin, Jianmin Bao, Zhuliang Yao, Qi Dai, and Han Hu. Simmim: A simple framework for masked image modeling. In *Proceedings of the IEEE/CVF conference on computer vision and pattern recognition*, pages 9653–9663, 2022. 3
- [51] Yifei Xin, Xiulian Peng, and Yan Lu. Masked audio modeling with clap and multi-objective learning. In *INTER-SPEECH*, pages 2763–2767, 2023. 2, 7
- [52] Jianwei Yang, Zhile Ren, Chuang Gan, Hongyuan Zhu, and Devi Parikh. Cross-channel communication networks. *Advances in Neural Information Processing Systems*, 32, 2019. 2
- [53] Xiang Zhang, Huiyuan Yang, Taoyue Wang, Xiaotian Li, and Lijun Yin. Multimodal channel-mixing: Channel and spatial masked autoencoder on facial action unit detection. In *Proceedings of the IEEE/CVF Winter Conference on Applications of Computer Vision*, pages 6077–6086, 2024. 2, 3, 4, 8
- [54] Daquan Zhou, Zhiding Yu, Enze Xie, Chaowei Xiao, Animeshree Anandkumar, Jiashi Feng, and Jose M Alvarez. Understanding the robustness in vision transformers. In *International Conference on Machine Learning*, pages 27378–27394. PMLR, 2022. 2
- [55] Jinghao Zhou, Chen Wei, Huiyu Wang, Wei Shen, Cihang Xie, Alan Yuille, and Tao Kong. ibot: Image bert pre-training with online tokenizer. *International Conference on Learning Representations (ICLR)*, 2022. 3, 6, 7, 1, 2
- [56] Xiaoxiang Zhu, Jingliang Hu, Chunping Qiu, Yilei Shi, Hossein Bagheri, Jian Kang, Hao Li, Lichao Mou, Guicheng Zhang, Matthias Häberle, Shiyao Han, Yuansheng Hua, Rong Huang, Lloyd Hughes, Yao Sun, Michael Schmitt, and Yuanyuan Wang. New: So2sat lcz42, 2019. 1, 3, 5, 6, 8, 2
- [57] Jian Zou, Tianyu Huang, Guanglei Yang, Zhenhua Guo, Tao Luo, Chun-Mei Feng, and Wangmeng Zuo. Unim 2 ae: Multi-modal masked autoencoders with unified 3d representation for 3d perception in autonomous driving. In *European Conference on Computer Vision*, pages 296–313. Springer, 2024. 1

ChA-MAEViT: Unifying Channel-Aware Masked Autoencoders and Multi-Channel Vision Transformers for Improved Cross-Channel Learning

Supplementary Material

6. Image patching

Formally, let $I \in \mathbb{R}^{h \times w \times c}$ represent a multi-channel input image, where (h, w) denotes the dimensions of the image and c is the number of channels. We begin by patchifying each channel into n 2-D patches of size $p \times p$ in pixels. This process yields $n \times c$ patches, denoted as $\mathbf{x}_{i,j} \in \mathbb{R}^{p \times p}$, where $n = \frac{h \cdot w}{p^2}$ is the number of patches per channel, i indicates the spatial location of a given patch, and j denotes the j -th channel. Next, we flatten each patch $\mathbf{x}_{i,j} \in \mathbb{R}^{p^2}$, and then pass it into a shared linear projection $\mathbf{W} \in \mathbb{R}^{p^2 \times d}$. This results in patch tokens $\mathbf{t}_{i,j} = (\mathbf{x}_{i,j} \cdot \mathbf{W}) \in \mathbb{R}^d$, leading to a sequence of $n \times c$ patch tokens $[\mathbf{t}_{1,1}; \mathbf{t}_{2,1}; \dots; \mathbf{t}_{n,c}]$.

7. Dynamic Channel-Patch (DCP) Masking Algorithm

Algorithm 1 outlines the procedure of Dynamic Channel-Patch (DCP) Masking in Sec. 3.1 of the main paper, where we combine both *patch* and *channel* masking strategies.

8. Combination of DiChaViT with SSL

We adopt the following SSL methods with DiChaViT [39] as baselines: SimCLR [10, 11], SimSiam [12], MAE [23], iBOT [55], and DINOv2 [38].

SimCLR [10, 11] utilizes augmentation strategies that include random cropping, color distortion, and Gaussian blur to generate the dual views of an input image. This approach requires twice the computational resources per sample compared to single-path methods. Since hue and saturation are not well defined in multi-channel images, we apply the augmentation by only adjusting brightness and contrast.

SimSiam [12] employs similar augmentations as SimCLR, but it eliminates the use of negative pairs by stop-gradient. This operation helps prevent representation collapse by decoupling the optimization of the twin network branches, which simulates an alternating optimization process similar to the Expectation-Maximization (EM) approach. Additionally, SimSiam does not require momentum encoders.

MAE [23] involves randomly masking a large portion of the input image and training the model to reconstruct the missing content. Unlike contrastive methods, MAE does not depend on augmentation pipelines, which can be ineffective for heterogeneous channels in MCI. Additionally, by processing only a small fraction of the image, this method

Algorithm 1: Dynamic Channel-Patch Masking

```
Input : Number of patches per channel  $n$ ;  
         Number of channels  $c$ ;  
         Patch mask ratio  $r_p$ ;  
         Probability of using patch masking  $p_{\text{patch}}$ ;  
         Probability of using channel masking  $p_{\text{channel}}$ ;  
         ( $0 \leq p_{\text{patch}} + p_{\text{channel}} \leq 1$ )  
  
// Random Patch Mask  
1 p_mask =  $\mathbf{0}^{n \times c}$  // initialize patch mask  
2 For  $j = 1, 2, \dots, c$ :  
3   p_mask $[:, j]$  = generate_mask( $n, r_p$ )  
4 EndFor  
// Dynamic Channel Mask  
5 Uniformly sample a number of channels to mask  
    $k \sim \mathcal{U}\{0, 1, \dots, c - 1\}$   
6 Uniformly sample  $k$  masked channels  
    $C' = \text{Sample}(\{1, \dots, c\}, k)$   
7 c_mask =  $\mathbf{0}^{n \times c}$  // initialize channel mask  
8 For  $j \in C'$ :  
9   c_mask $[:, j]$  =  $\mathbf{1}^n$  // mask whole channel  $j$   
10 EndFor  
// Masks For Current Iteration  
11 Sample  $s \sim \mathcal{U}(0, 1) \in \mathbb{R}$   
12 If  $s < p_{\text{patch}}$ :  
13   mask = p_mask // Using patch mask  
14 Else If  $s < p_{\text{patch}} + p_{\text{channel}}$ :  
15   mask = c_mask // Using channel mask  
16 Else: // Combining both masks  
17   mask = p_mask  $\vee$  c_mask  
Output : mask  $\in \{0, 1\}^{n \times c}$ , where 1 denotes mask
```

significantly lowers computational demands, thereby enhancing efficiency.

iBOT [55] combines masked image modeling with self-distillation by utilizing dual augmentation streams that include both masked and full views. This encourages the model to align representations across different views while reconstructing missing content. Particularly, iBOT uses clockwise masking introduced in BEiT [4], where a block of image patches is masked each time. To adapt this clockwise masking for multi-channel images, we generate a mask for each channel, ensuring that the masked blocks only cover the areas in the channel. Compared to MAE, iBOT introduces additional computational overhead due to its use of teacher-student distillation. Furthermore, the dual-stream processing increases the per-sample training cost, making iBOT more computationally demanding than single-view methods like MAEs.

DINOv2 [38] employs multi-cropping alongside various augmentations, such as color jittering, Gaussian blur, and random solarization, as well as self-distillation techniques. Notably, DINOv2 also incorporates additional loss functions, such as iBOT loss [55] and KoLeo loss [43]. During training, DINOv2 generates multiple crops from each image (e.g., 2 global views and 8 local views) which leads to significantly higher computational demands compared to other SSL methods. For example, training DINOv2 on the CHAMMI dataset using a single GPU requires approximately 5 days, whereas SimCLR takes around 2 days and MAE only requires 1 day.

To integrate these SSL methods with DiChaViT [39], we add the task loss and optimize it along with the SSL loss. Additionally, we explored another variant that included an additional branch utilizing standard augmentations recommended by the authors of the dataset to optimize the task loss and return the predictions at test time (e.g., only using random cropping, horizontal flipping, and thin-plate-spline transformation [16] for CHAMMI). We observed that relying exclusively on complex augmentation pipelines, like those used in SimCLR, negatively impacts the performance of the combined model, while incorporating at least one view with regular augmentation enhances the model’s learning capability. For self-distillation methods such as DINOv2, we found that the performance of the teacher network is slightly better than that of the student network, thus we report the performance on the teacher network.

9. Implementation details

We employ a ViT small architecture with 21M parameters as the backbone for all methods. To ensure that we maintain the same number of parameters as the baselines, we removed one layer from the encoder to incorporate it into the decoder for our method. For both CHAMMI and JUMP-CP, we use a patch size of 16, while for the So2Sat dataset, we opt for a patch size of 8. We trained the models using the AdamW optimizer, aiming to minimize the cross-entropy loss for the JUMP-CP and So2Sat datasets, while employing proxy loss for CHAMMI.

CHAMMI dataset [13]. For the baselines, we utilize the [CLS] token from the final layer as the feature representation and train the model to minimize the proxy loss [48]. We then evaluate the model on various tasks using the evaluation code provided by [13], incorporating a 1-Nearest Neighbour classifier to calculate the macro-average F1-score for each task individually⁴. The channel-adaptive interfaces are adapted from the authors’ implementation code⁵. In addition to the model, we apply the same data

⁴<https://github.com/broadinstitute/MorphEm>

⁵https://github.com/chaudatascience/channel_adaptive_models

augmentation techniques recommended by the authors, including thin-plate-spline (TPS) transformations [16]. Each model is trained for 100 epochs with a learning rate of 0.00004 and a batch size of 64.

JUMP-CP [8] and So2Sat [56] datasets. Following [5, 39], we warm up the learning rate for the first 10 epochs, reaching a peak of 0.0005. After this initial period, the learning rate gradually decays to 10^{-6} according to a cosine scheduler. To mitigate overfitting, we apply a weight decay of 0.04 to the weight parameters while excluding the bias and normalization terms. We use the same data augmentation techniques as outlined in [39]. For the final prediction, we utilize [CLS] token from the Transformer encoder into a classifier head to predict the probability of each class. Each model is trained for 100 epochs, with a batch size of 64 on JUMP-CP and 128 on So2Sat.

Compute resources. Experiments conducted on So2Sat and CHAMMI utilize one NVIDIA RTX GPU with 48GB RAM, alongside three Intel(R) Xeon(R) Gold 6226R CPUs. For JUMP-CP experiments, two NVIDIA RTX GPUs and six Intel(R) Xeon(R) Gold 6226R CPUs were used.

10. Additional Results and Analyses

10.1. CHAMMI Benchmark Results

Tab. 6 presents the F1 scores of various MCI-ViT models (ViT-S backbone) evaluated on the CHAMMI benchmark [13]. The evaluation consists of nine tasks, including six out-of-distribution (OOD) tasks. ChA-MAEViT demonstrates superior overall performance, achieving the highest scores in six out of the nine tasks across different settings.

10.2. Performance when only using SSL Objectives

We evaluate the effectiveness of ChA-MAEViT in the SSL setting by comparing the performance of different SSL methods. Specifically, all models were trained solely using SSL objectives, *i.e.*, no task-specific loss was incorporated. For the So2Sat [56] and JUMP-CP [8] datasets, we reported the accuracy from linear probing over 20 epochs. As shown in Fig. 6, ChA-MAEViT achieves the highest score of 37.7%, surpassing other approaches by 1.0 – 8.5% on CHAMMI. In Fig. 7, our method consistently outperforms baseline models in both Full and Partial settings on So2Sat. A similar trend is observed for JUMP-CP in Fig. 8. This demonstrates the effectiveness of our method in SSL settings for MCI, highlighting its ability to extract meaningful representations in scenarios where supervised labels are unavailable.

10.3. Leave-One-Channel-Out at Test Time

In Tab. 7, we present the results of training the model using all eight channels of JUMP-CP and then testing it with

Model	Average OOD				WTC		HPA			CP			
	Mean	WTC	HPA	CP	Task1	Task2	Task1	Task2	Task3	Task1	Task2	Task3	Task4
HyperNetViT [22]	47.17	45.78	67.61	28.11	58.83	45.78	88.78	82.70	52.52	82.13	53.74	23.16	7.42
DepthwiseViT [13]	50.44	52.19	71.41	27.72	69.81	52.19	91.65	88.04	54.78	81.24	54.08	23.21	5.87
TempMixingViT [40, 41, 44]	47.33	51.52	64.80	25.66	61.66	51.52	85.01	79.91	49.69	77.45	48.83	22.56	5.60
CA-MAE [28] + Sup. Loss	48.82	61.85	56.45	28.15	77.57	61.85	84.45	71.89	41.01	76.49	56.52	19.43	8.49
ChAda-ViT [6]	50.82	67.18	60.67	24.60	77.58	67.18	87.49	75.94	45.41	83.92	45.58	21.94	6.28
ChannelViT [5]	52.54	67.58	62.35	27.81	78.36	67.58	83.93	76.73	47.97	77.70	55.16	21.89	6.38
DiChaViT [39]	55.36	75.18	64.36	26.53	80.87	75.18	88.08	79.26	49.45	84.08	53.03	20.95	5.60
ChA-MAEViT (ours)	58.71	77.15	72.11	26.87	84.52	77.15	94.14	87.47	56.75	90.89	57.68	14.99	7.95

Table 6. **F1 Scores of MCI-ViT models on CHAMMI benchmark [13]**. ChA-MAEViT demonstrates better overall performance on CHAMMI, achieving the highest scores in 6 out of 9 tasks across various settings. “OOD” refers to out-of-distribution tasks. All models have the same number of parameters, except CA-MAE with 3X more parameters due to its use of separate decoders.

Missing channel at inference	ChannelViT [5]	DiChaViT [39]	ChA-MAEViT (ours)
0	61.72 ± 0.48	63.48 ± 0.20	86.29 ± 0.37
1	61.21 ± 0.41	62.72 ± 0.28	86.16 ± 0.32
2	61.90 ± 0.48	63.28 ± 0.31	87.13 ± 0.24
3	37.70 ± 0.60	38.83 ± 0.46	61.79 ± 0.58
4	58.52 ± 0.63	59.61 ± 0.17	82.67 ± 0.53
5	67.28 ± 0.53	69.12 ± 0.16	89.24 ± 0.35
6	67.20 ± 0.59	69.06 ± 0.20	87.54 ± 0.20
7	67.37 ± 0.60	69.21 ± 0.19	86.03 ± 0.32

Table 7. **Analysis of Leave-One-Channel-Out Testing**. We present the detailed results for column “7” in Table 3 from the main paper. Each row shows the results obtained by leaving out one channel and testing the model on the remaining seven channels. For all experiments conducted, we provide the *mean ± standard deviation* based on three runs. Our method, ChA-MAEViT, consistently outperforms the best two baselines ChannelViT [5] and DiChaViT [39] by 17 – 23% across all tested combinations.

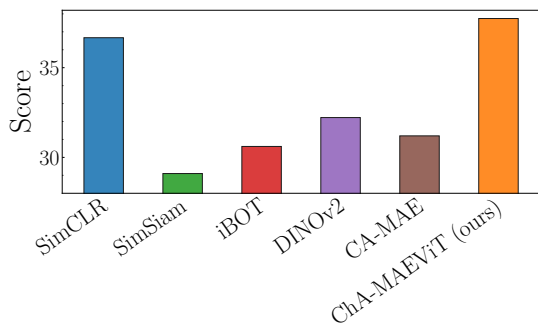


Figure 6. **Comparison of SSL methods on CHAMMI [13]**. All models were trained solely using SSL objectives, *i.e.*, without any task loss. ChA-MAEViT achieves the highest score, outperforming other baselines by 1.0 – 8.5%, demonstrating the effectiveness of our approach over other methods in SSL settings for MCI.

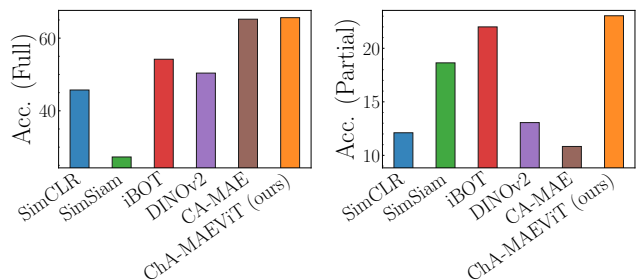


Figure 7. **Comparison of SSL methods on So2Sat [56]**. All models were trained solely using SSL objectives, *i.e.*, without any task loss, then trained with linear probing for another 20 epochs. ChA-MAEViT outperforms other baselines in both Full (left) and Partial channel settings (right), demonstrating its effectiveness for SSL in both scenarios.

various combinations of seven channels. This provides a detailed result for column “7” of Tab. 3 in the main paper, which represents $C_8^7 = 8$ different channel combinations. For each combination, we report the mean and standard de-

viation of the model’s performance based on three runs. Our results demonstrate that ChA-MAEViT achieves an improvement of 17 – 23% for each combination compared to the baseline models DiChaViT [39] and ChannelViT [5].

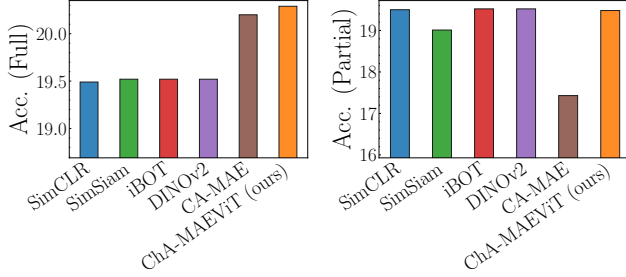


Figure 8. **Comparison of SSL methods on JUMP-CP [8].** All models were trained solely using SSL objectives, *i.e.*, without any task loss, then trained with linear probing for another 20 epochs. ChA-MAEViT achieves the highest score when tested on Full channels (left) and performs comparably to the top-performing baselines on Partial channel settings (right).

10.4. Dynamic Channel-Patch (DCP) Masking Analysis

DCP Combination with varying masking ratios r_p . Fig. 9 shows the impact of varying *random patch masking ratios* (r_p) on the performance of ChA-MAEViT when trained with DCP Combination ($p_{\text{patch}} = p_{\text{channel}} = 0$). The blue and purple lines indicate the performance for full and partial channels on JUMP-CP, respectively. As the masking ratio r_p increases, accuracy for both full and partial channels decreases due to excessive information loss, making reconstruction more difficult. Since DCP Combination masks both patches and channels, it is reasonable to use a small r_p , in contrast to previous studies that often utilize a high ratio (*e.g.*, 0.75). The best performance is observed at $r_p = 0.25$ for JUMP-CP.

DCP Alternate with varying proportions of p_{channel} and p_{patch} . Fig. 10 evaluates the performance of *DCP Alternate* in ChA-MAEViT by varying the proportions of *channel-* and *patch-* level masking. We adjust p_{channel} , while setting $p_{\text{patch}} = 1 - p_{\text{channel}}$ to control the contribution of each masking strategy. For example, $p_{\text{channel}} = 1$ indicates exclusive channel-level masking, and $p_{\text{channel}} = 0$ denotes only using patch-level masking. The blue and purple lines represent accuracy on JUMP-CP for Full and Partial channel settings, respectively, across different p_{channel} values. We observed that using both channel and patch masks together improves performance. Additionally, a higher channel-level masking proportion (*i.e.*, larger p_{channel}) improves accuracy in the Partial setting (purple) but leads to a decline in the Full setting (blue), highlighting the trade-off between these masking strategies.

Patch Masking Strategies in DCP. Fig. 11 compares two patch masking strategies with DCP. The first strategy, *Duplicate-Spatial Mask*, creates a patch mask for one channel and then duplicates the mask across all other channels (*e.g.*, [36, 49]). The second approach, *Independent-Spatial*

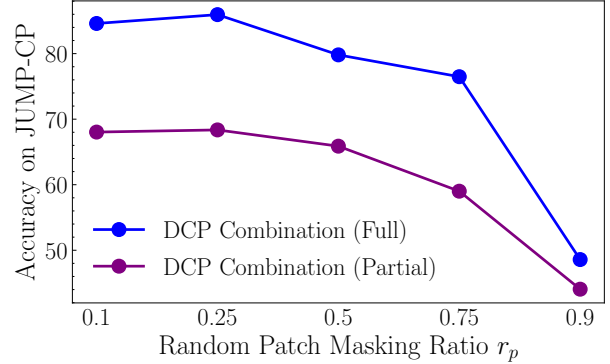


Figure 9. **DCP Combination with varying masking ratios r_p .** We train ChA-MAEViT using a combined mask integrating both channel- and patch-level masking, *i.e.*, *DCP Combination* ($p_{\text{channel}} = p_{\text{patch}} = 0$). The blue and purple lines depict accuracy on JUMP-CP for Full and Partial channel settings, respectively, across different patch masking ratios r_p .

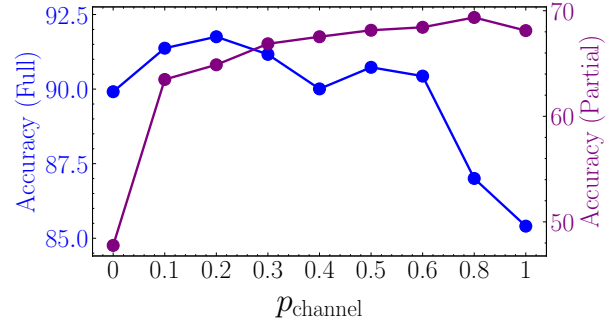


Figure 10. **DCP Alternate with different proportions of p_{channel} and p_{patch} .** To evaluate the effects of *channel-* and *patch-* level masks in ChA-MAEViT during alternating masking, we vary p_{channel} while setting $p_{\text{patch}} = 1 - p_{\text{channel}}$. $p_{\text{channel}} = 1$ indicates only using channel-level masking, whereas $p_{\text{channel}} = 0$ indicates only using patch-level masking. The blue and purple lines represent accuracy on JUMP-CP for Full and Partial channel settings respectively, across different values of p_{channel} .

Mask, generates a patch mask for each channel independently, resulting in varied patch positions. We set the same masking ratio for both strategies. Our findings indicate that using a different mask for each channel performs better than the duplicating one, yielding an improvement of 1.2–5.5% across three datasets.

10.5. Memory Token Analysis

Memory Token Attention. Fig. 12 shows the attention patterns between image patches and memory tokens of the encoder. Each group of channels displays distinct preferences for specific memory tokens. Fig. 12(a) shows that the *VH* channels primarily focus on memory token 1, while the *Lee-*

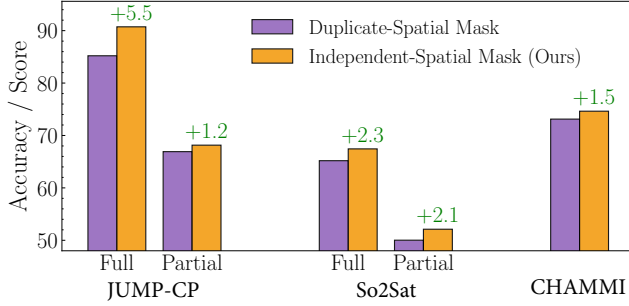


Figure 11. **Patch Masking Strategies in DCP.** We observed that using a different mask for each channel outperforms duplicating the same mask across all channels (purple), resulting in improvements of 1.2 – 5.5% across three datasets.

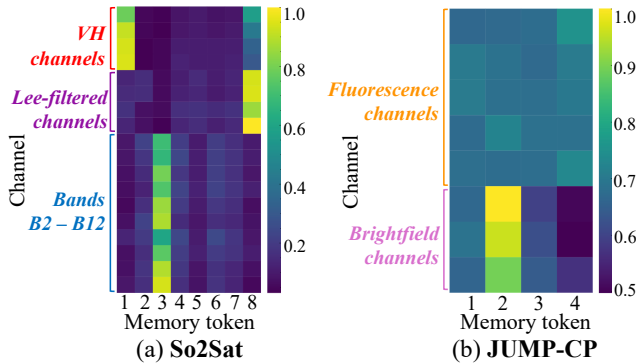


Figure 12. **Attention between image patches and memory tokens of the encoder on the test set of So2Sat and JUMP-CP.** Each channel group focuses on different memory tokens. For example, on (a) So2Sat, *VH* channels utilize memory token 1, whereas *Lee-filtered* channels pay more attention to memory token 8.

filtered channels have stronger attention toward memory token 8. Similarly, for JUMP-CP in Fig. 12(b), the *Brightfield* channels allocate more attention to memory token 2, whereas *Fluorescence* channels show a slight preference for memory token 4. This suggests that each type of channel utilizes different memory tokens to store the global information necessary for feature extraction.

Impact of memory tokens on reconstruction loss. Fig. 13 shows the effect of memory tokens on reconstruction loss during training. Evaluated on the So2Sat dataset, the model using memory tokens (blue line) achieves lower and smoother loss compared to those without them (red). This indicates that memory tokens may improve the model’s ability to capture global information, helping to ease the learning process.

10.6. Number of Decoder Blocks of ChA-MAEViT

Fig. 14 illustrates the performance of ChA-MAEViT when trained on the So2Sat dataset with varying numbers of de-

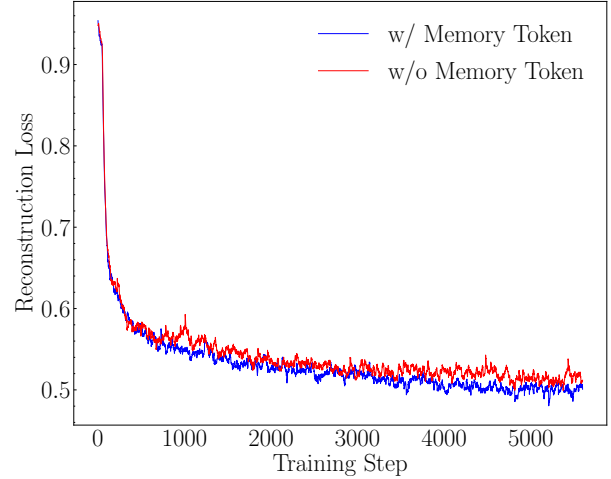


Figure 13. **Impact of memory tokens on the reconstruction loss.** Using memory tokens helps the reconstruction task, as demonstrated by the lower reconstruction loss observed on So2Sat.

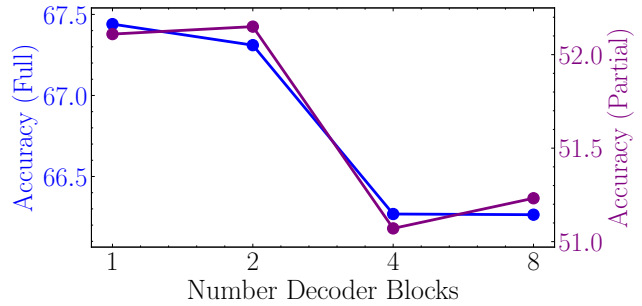


Figure 14. **Number of Decoder Blocks of ChA-MAEViT.** We show the performance of ChA-MAEViT when trained on So2Sat with different numbers of blocks in the decoder. We observed that using 1 – 2 blocks gives the best performance.

coder blocks. We found that a configuration of 1 to 2 blocks yields the best performance.

10.7. Scaling Model Size

Tab. 8 compares the performance of ChA-MAEViT with the two strongest supervised baselines: ChannelViT [5] and DiChaViT [39]. To evaluate the impact of model scaling, each model is evaluated using two backbone architectures: ViT-S (21M parameters) and ViT-B (85M parameters). Larger models exhibit improved performance, particularly on CHAMMI and JUMP-CP. Our approach consistently outperforms the baselines across all three datasets, regardless of the backbone used. In ChA-MAEViT, we reallocate one Transformer block from the encoder to the decoder, ensuring that all models maintain the same parameter count.

Model	Backbone	CHAMMI [13]	JUMP-CP [8]		So2Sat [56]	
		Avg score	Full	Partial	Full	Partial
ChannelViT [5]	ViT-S	64.97	67.51	56.49	61.03	46.16
DiChaViT [39]	ViT-S	69.77	69.19	57.98	63.36	47.76
ChA-MAEViT (ours)	ViT-S	74.63	90.73	68.15	67.44	52.11
ChannelViT [5]	ViT-B	67.72	67.92	56.97	62.19	46.20
DiChaViT [39]	ViT-B	70.56	69.47	58.33	63.93	47.92
ChA-MAEViT (ours)	ViT-B	77.09	92.22	70.24	67.67	52.27

Table 8. **Scaling Model Size.** We compare ChA-MAEViT with the two best baseline models, ChannelViT [5] and DiChaViT [39]. Each model is evaluated using two backbones: ViT-S (21M parameters) and ViT-B (85M parameters). Increasing the model size boosts performance, particularly on CHAMMI and JUMP-CP. Our method outperforms others across three datasets with both backbones.

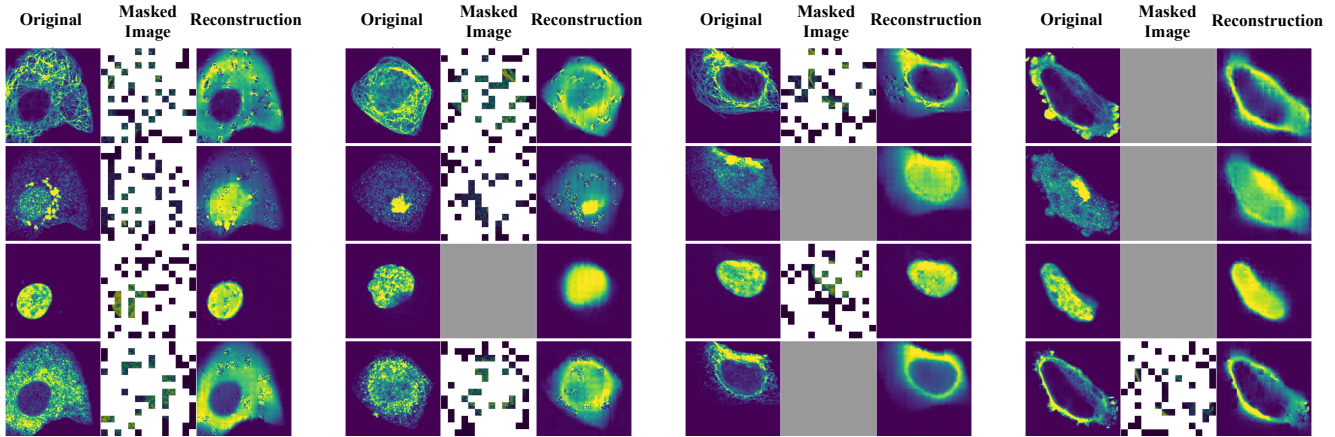


Figure 15. **Visualization of original, masked, and reconstructed images on CHAMMI-HPA [13], which contains 4 channels.** We show the reconstruction of ChA-MAEViT, utilizing a ViT-S/16 backbone. ChA-MAEViT demonstrates its capability to effectively reconstruct masked channels and patches under different channel masking settings (0 – 3 masked channels with a fixed $patch\ masking\ ratio\ r_p = 75\%$). Gray blocks indicate fully masked channels.

10.8. Reconstruction Images

Fig. 15 shows the *original*, *masked*, and *reconstructed* images from the CHAMMI-HPA dataset [13], which contains four channels. Each set of images shows the original image on the left, followed by the masked image created using Dynamic Channel-Patch Masking (with patch masking ratio $r_p = 75\%$), and finally, the reconstructed image produced by ChA-MAEViT (utilizing a ViT-S/16 backbone) on the right. The gray blocks indicate the entire channel has been masked. ChA-MAEViT demonstrates its ability to leverage cross-channel dependencies as it can reconstruct the entire channels using available patches from the other channels.

10.9. Novel Channels at Inference

For the novel channels setting, we trained ChA-MAEViT using the first three channels (*i.e.*, channels 0, 1, 2) and then tested it on two other channels (*i.e.*, channels 3, 4) of JUMP-CP. One of the main challenges is that new channels do not

have learned *channel tokens*. To address this, we assume that some unlabeled test images are available at test time. We initialize the channel tokens for the new channels randomly and then fine-tuned these channel tokens on the unlabeled test images using the reconstruction loss in Eq. (4). Throughout this process, we kept the entire model frozen and only fine-tuned the newly initialized channel tokens.

In Fig. 16, we illustrate the accuracy on novel channels with varying numbers of unlabeled test images. For example, “0” indicates that no fine-tuning was performed, while “8” represents that eight test images (each containing only the two novel channels) were used to fine-tune the channel tokens before testing the model on the remaining test set. We observed that fine-tuning the channel tokens with some unlabeled test images improved performance from 9.2% (without fine-tuning) to 11.6% (with fine-tuning on 640 unlabeled test images). Additionally, to make an upper performance bound, we trained ChA-MAEViT on the training set of the novel channels (*i.e.*, channels 3 and 4).

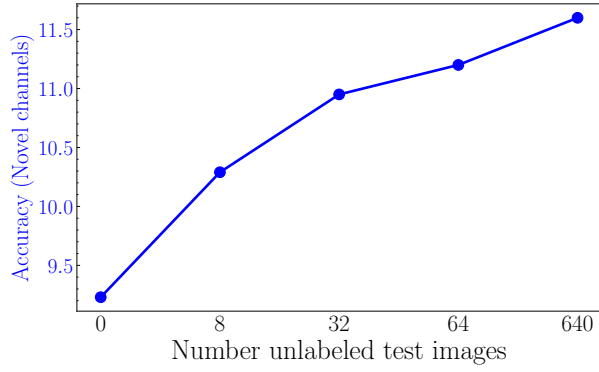


Figure 16. **Novel Channels at Inference.** Fine-tuning the *channel tokens* of novel channels with unlabeled test images boosted performance from 9.2% (without fine-tuning, denoted as “0”) to 11.6% (with fine-tuning on 640 unlabeled test images).

This model achieved an accuracy of 46.1%, indicating there is still a significant performance gap which we leave for future work.